Spin reorientation and sign reversal of Berry curvature induced intrinsic anomalous Hall effect in the manganese pnictide MnSb

Nisha Shahi, Gaurav K. Shukla, Vishal Kumar, and Sanjay Singh*
School of Materials Science and Technology, Indian Institute of Technology (Banaras Hindu University), Varanasi 221005, India

(Received 23 February 2024; revised 7 June 2024; accepted 13 June 2024; published 27 June 2024)

The manipulation of the anomalous Hall effect (AHE) by controlling magnetization is of great interest in condensed matter physics due to its potential application for the practical design of spintronic devices. In this study, we report a combined experimental and theoretical investigation of the AHE in the MnSb manganese pnictide. Temperature-dependent magnetization measurement indicates spin reorientation transition (SRT) temperature at $\sim$ 120 K (T_{SR}). Magnetotransport data shows that negative magnetoresistance increases from room temperature up to SRT temperature 120 K, then decreases and becomes positive at very low temperatures. The anomalous Hall conductivity (AHC) shows temperature-independent behavior from room temperature to T_{SR} followed by a drop and sign reversal at low temperatures. Detailed scaling analysis of anomalous Hall data suggests that the AHE above T_{SR} is primarily governed by the intrinsic Berry curvature and the obtained value of intrinsic AHC is about 310 S/cm. In contrast, below $T_{SR,}$ the extrinsic skew scattering becomes the dominant contributor to the AHE compared to the intrinsic Berry curvature and the obtained value of intrinsic AHC is about–28 S/cm. The first-principles calculations reveal that changes in the sign and magnitude of the intrinsic AHC are attributed to modifications in the Berry curvature when the magnetic moment undergoes rotation from the *c*-axis to the *ab*-plane. Our study yields a compound exhibiting large AHC and offers an insightful comprehension of the anisotropic behavior of AHE due to the modification of Berry curvature.

DOI: 10.1103/PhysRevB.109.245136

I. INTRODUCTION

The anomalous Hall effect (AHE) describes the appearance of additional Hall voltage in the magnetic materials due to the interplay between the magnetization and spin-orbit coupling (SOC) [1–3]. The AHE is valuable for spintronics, characterizing magnetization in small devices, and developing materials for data storage, magnetic sensors, and magnetoresistive random-access memory by enabling electron spin measurement and manipulation [1,2,4–6]. The AHE arises as a result of two qualitatively different microscopic mechanisms, an extrinsic mechanism that includes skew scattering and side jump, and an intrinsic mechanism that is related to the effect of SOC on the band structure of materials [1,2,7–9].

The skew scattering and side jump mechanisms are described as the asymmetric scattering and sudden transverse jump in the propagation direction of an electronic wave from spin-orbit coupled magnetic impurities, respectively, which creates extrinsic AHE in the system [10,11]. The intrinsic mechanism is independent of any kind of scattering, unlike the extrinsic mechanism, and merely depends on the electronic band structure of the material [1]. The intrinsic mechanism was first proposed by Karplus and Luttinger in terms of the anomalous velocity of electrons due to the effect of SOC on the band structure [12], and later it was formulated in terms of the Berry curvature associated with Bloch bands [2]. The Berry curvature acts as a pseudomagnetic field in the momentum space and leads to the intrinsic AHE [1,2,12–15]. The Berry curvature significantly enhances wherever two electronic bands approach each other energetically and hybridize as a consequence of the combined effect of SOC and broken time-reversal symmetry [16–18]. The interband mixing under the influence of SOC may create band degeneracy or band splitting, and when the Fermi level resides within the SOC-induced band splitting, the Berry curvature experiences a sharp enhancement [16,19–21]. Binary compounds such as Mn_3Sn [9], Mn_3Ge [22], Fe_3Sn_2 [23–26], Fe_5Sn_3 [27], and Mn_3Pt [28] show a large AHE due to the nonvanishing Berry curvature associated with the nontrivial electronic band structure. Recently, extensive research has been carried out to unravel the sign reversal of AHE due to many factors such as spin orientation [28–31], the value of magnetization [32], and the interface-induced SOC or breaking inversion symmetry [33].

The Mn pnictides such as MnBi, MnSb, and MnAs with NiAs-type hexagonal structure have gained renewed recognition in high-temperature spintronics research due to their peculiar band structure, high Curie temperature, spin reorientation transition (SRT), and large uniaxial magnetocrystalline anisotropy with the magnetic easy axis parallel to the *c*-axis of the crystal system [34–41]. A most recent study on the MnAs compound demonstrated the SOC-induced band splitting and enhanced intrinsic anomalous Hall conductivity (AHC) depending on the magnetization orientation [19,20]. A neutron diffraction study [40] and a recent magnetotransport study [37] in a composition close to MnSb indicates the presence of SRT and AHE, respectively. Nevertheless, the influence

*Contact author: ssingh.mst@iitbhu.ac.in

of SRT on the electronic band structure and its consequent impact on AHE is missing in the literature.

In this work, we present a comprehensive study of the AHE in the MnSb compound through experimental and theoretical approaches. Temperature-dependent magnetization data indicates a magnetic transition at ∼120 K, which is expected due to the SRT [40]. Magnetotransport data indicates that negative magnetoresistance (M.R.) first increases from room temperature to the SRT temperature (T_{SR}) ∼120 K, and afterward decreases and becomes positive in a very-low-temperature region. The AHC shows temperature-independent behavior from room temperature to T_{SR}, followed by a drop and sign reversal at low temperatures. A detailed scaling analysis of anomalous Hall data indicates that the intrinsic Berry curvature is predominantly responsible for the AHE above T_{SR} and the obtained value of the intrinsic AHC is about 310 S/cm. However, below T_{SR}, the AHE is mainly governed by the extrinsic skew scattering mechanism and the obtained value of the intrinsic AHC is about–28 S/cm. First-principles calculations reveal that changes in the sign and magnitude of intrinsic AHC originated from the modification in Berry curvature linked with the band splitting near the Fermi level. The modification in Berry curvature arises due to the reconstruction of the electronic band structure when the magnetic moment undergoes rotation from the *c*-axis to the *ab*-plane.

II. METHODS

The polycrystalline MnSb binary compound is prepared by the standard arc-melting method [42,43]. The constituent elements (purity higher than 99.9%) of the intermetallic system are melted in a water-cooled copper hearth under argon atmosphere (purity better than 99.999%). The sample is remelted 5 times to ensure homogeneous mixing of the constituents. A negligible weight loss of 1% was noticed after the melting of the sample. The obtained ingot was then vacuum sealed in a quartz tube, followed by annealing at 1073 K for three days to achieve good homogeneity. The chemical composition is verified using the energy dispersive analysis of x-ray technique. The average composition is found to be $Mn_{0.99}Sb_{1.00}$, which corresponds to MnSb. A small piece of the sample is powdered, and room temperature x-ray diffraction (XRD) is performed in the Rigaku X-ray diffractometer (wavelength ∼1.54 Å) for structural analysis. The direct current magnetization measurements are performed using a physical property measurement system (PPMS) and the Magnetic Properties Measurement System (MPMS) of quantum design. The polished rectangular piece of the dimension $4 \times 2 \times 0.7\ mm^3$ was used for temperature and magnetic field–dependent transport measurements using a cryogen-free measurement system (Cryogenic, CFMS). The transport measurements are performed by the four-probe method. To remove the longitudinal resistivity contribution in the Hall data due to voltage probe misalignment, we have antisymmetrized the Hall resistivity data by using the formula $\rho_{xy} = [\rho_{xy}(+H) - \rho_{xy}(-H)]/2$. However, we have symmetrized the M.R. data by using the formula $\rho_{xy} = [\rho_{xy}(+H) + \rho_{xy}(-H)]/2$ to remove the transverse resistivity contribution in the M.R.

The electronic band structure and magnetic properties of the MnSb compound were calculated by employing pseudopotential (PP)-based density-functional theory and plane-wave basis sets as implemented in QUANTUM ESPRESSO (QE) [44], whereas exchange-correlation potential is approximated by a Perdew-Burke-Ernzerhof generalized gradient approximation approach [45] through optimized Norm-conversing Vanderbilt PPs [46]. The kinetic energy cutoff of 80 Ry is used for the calculation. The Gaussian smearing value (0.01 Ry) is used both for the self-consistent (SC) and non-self-consistent (NSC) calculations to carry out electronic integration over the Brillouin zone (BZ). We have used the WANNIER90 tool (implemented within QE) to compute the Wannier interpolated bands, Berry curvature, and AHC [44,47–49]. The Monkhorst-Pack **k**-grid of $8 \times 8 \times 8$ of the BZ is considered for calculations, namely SC, NSC, and WANNIER90. We found that the Mn *d*-orbitals and Sb *p*-orbitals used as the projection for the WANNIER90 calculations provide good interpolation. A denser BZ **k**-grid of $100 \times 100 \times 100$ is taken to calculate the intrinsic AHC. Through the adaptive refinement technique, a further fine mesh of $5 \times 5 \times 5$ is added around the points wherever the mode of the Berry curvature ($|\Omega(\mathbf{k})|$) exceeds 100 $bohr^2$. The calculations are carried out by using the refined lattice parameters obtained from the experiment.

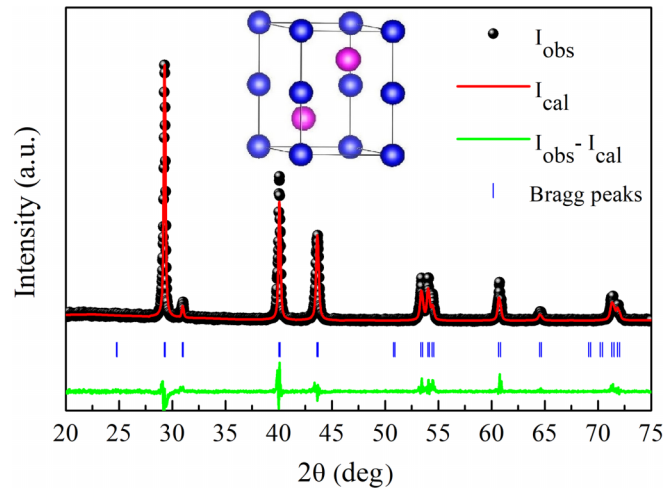

FIG. 1. Rietveld profile fitting of the room temperature XRD pattern of the MnSb compound. The observed (I_{obs}), calculated (I_{cal}), and the difference between observed and calculated profiles ($I_{obs} - I_{cal}$) are shown by black sphere, red continuous line, and green continuous line, respectively. The blue tick bars indicate the Bragg peak positions. The inset displays crystal structure of MnSb. The blue and magenta spheres indicate the Mn and Sb atoms, respectively.

III. RESULTS AND DISCUSSION

A. Structural characterization

The XRD data at room temperature was collected to investigate the crystal structure of the MnSb. We performed Rietveld refinement of the XRD data considering a hexagonal structure with space group $P6_3/mmc$ (Fig. 1) as reported in the literature [50,51]. The refinement was performed using the FULLPROF software package [52]. In the refinement, the Mn and Sb atoms were considered at 2a (0, 0, 0) and 2c (0.67, 0.33, 0.75) Wyckoff positions, respectively. It can be

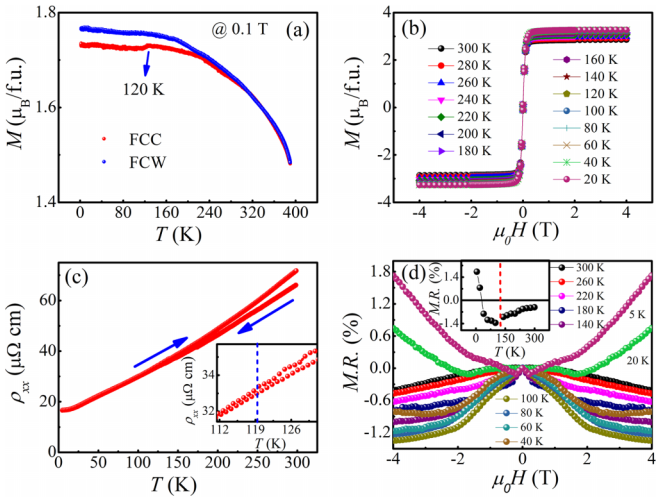

FIG. 2. (a) Temperature-dependent magnetization curve at 0.1 T. (b) Isothermal field-dependent magnetization at different temperatures. (c) Resistivity (ρ_{xx}) versus temperature (T) plot in the cooling and heating sequence. The inset shows a zoomed view of the ρ_{xx} versus T data around SRT. (d) Plot of M.R. at different temperatures. The inset shows the variation of M.R. at 4 T as a function of temperature.

noticed from Fig. 1 that the observed and calculated peak profiles match well with each other, and there is no evidence of any impurity peaks in the XRD pattern, which suggests that the MnSb compound crystallizes in a single-phase hexagonal structure. The refined lattice parameters a and c are found to be ∼4.14 Å and ∼5.76 Å, which are in good agreement with the literature [50]. The inset of Fig. 1 shows the crystal structure of MnSb, built-in VESTA software [53].

B. Magnetization and resistivity measurements

The temperature variation of magnetization [$M(T)$] data [Fig. 2(a)] was recorded in a temperature range of 2 –390 K under a 0.1 T magnetic field in field cooled cooling (FCC) and field cooled warming (FCW) protocols. The $M(T)$ curve shows a magnetic transition around 120 K shown by an arrow in blue color. A magnetic transition close to 120 K has been observed previously in a similar composition, and this transition has been assigned as the SRT through neutron diffraction study [40]. The reported neutron diffraction study indicates that the spin associated with Mn atoms changes its orientation from the magnetic easy axis parallel to the c-axis to the ab-plane at low temperatures. Figure 2(b) presents the field-dependent magnetic isotherms in the temperature range of 20–300 K. The negligible hysteresis is due to the soft magnetic nature of the MnSb compound. The saturation magnetization of the present compound is found to be ∼3.3 μ_B/f.u. at 20 K, which agrees well the value reported in the literature [54–56].

Figure 2(c) shows the monotonous increase in the longitudinal resistivity with temperature, which illustrates the metallic behavior of the present compound. We have collected the resistivity data in both cooling and heating mode of temperature variation, which exhibits a thermal hysteresis above T_{SR} ∼120 K. The thermal hysteresis in the pre-SRT region confirms the thermally driven and first-order nature of spin reorientation phase transition [57,58]. Fig. 2(d) displays the M.R. at different temperatures calculated by performing the field-dependent resistivity measurement. The M.R. is calculated by using the following relation [41]:

$$\text{M.R.} = \frac{\rho_{xx}(H) - \rho_{xx}(0)}{\rho_{xx}(0)}, \tag{1}$$

where ρ_{xx}(H) and ρ_{xx}(0) are longitudinal resistivities at a particular field and zero field, respectively. The maximum value of M.R. is ∼1.7% at temperature 20 K. The inset of Fig. 2(d) indicates that the negative M.R. at 4 T increases with the lowering of the temperature, but below T_{SR}, it started to decrease and becomes positive in a very-low-temperature region, which might be originated from the spin orientation from the c-axis to the ab-plane below T_{SR}, as a similar unusual behavior of M.R. is anticipated around the SRT [25,28,59,60]. In the high-temperature region above T_{SR}, the orientation of spin associated with the Mn atom is restricted along the easy axis, i.e., the c-axis, and upon the application of a magnetic field the fluctuations of magnetic moments decrease, which may give rise to negative M.R [28,59]. However, in a low-temperature region below T_{SR}, the negative M.R. decreases and becomes positive at very low temperatures, which might be related to the orientation of Mn spin in the ab-plane or out of the direction of the easy axis. The spin oriented out of the direction of the easy axis may experience an increase in fluctuations on the application of a magnetic field and give rise to positive M.R. [28,59,61]. The literature suggests exotic effects of the spin reorientation on the Hall effect such as manipulation of the sign and magnitude of the AHE as a function of temperature [28–31]. Therefore, further, we investigated the Hall effect in the MnSb compound.

C. Anomalous Hall measurement

The Hall resistivity (ρ_{xy}) data was recorded in the temperature range of 20–300 K and the magnetic field up to ±4 T. The separate plots for ρ_{xy} above and below T_{SR} are shown in Fig. 3(a) and the inset of Fig. 3(a), respectively. Above the T_{SR}, the ρ_{xy} is positive, whereas it turns negative below T_{SR}. In general ρ_{xy} consists of two parts, namely ordinary Hall and anomalous Hall, and can be written as [26,62]

$$\rho_{xy} = R_0 H + R_s M_s, \tag{2}$$

where R_0 and R_s are the ordinary and anomalous Hall coefficients, respectively. M_s corresponds to the saturation magnetization, and R_sM_s represents the magnitude of anomalous Hall resistivity (ρ_{AH}). The ρ_{xy} increases steeply up to the ∼1 T field, which is observed due to the presence of AHE. At the higher field region (> 1 T), ρ_{xy} changes linearly and shows a positive slope with the magnetic field, which is due to the ordinary Hall effect [63]. To separate the ordinary and anomalous Hall contributions, we performed fitting of the ρ_{xy} versus H data by using Eq. (2) in the higher field region (> 1 T). The fitting of the ρ_{xy} versus H at different temperatures provides the value of R_0 and R_sM_s that corresponds to the slope and intercept of the fitted line. The temperature variation of R_0 is shown in Fig. 3(b). The high field Hall resistivity data tend to be nearly flat above 200 K [see Fig. 3(a)],

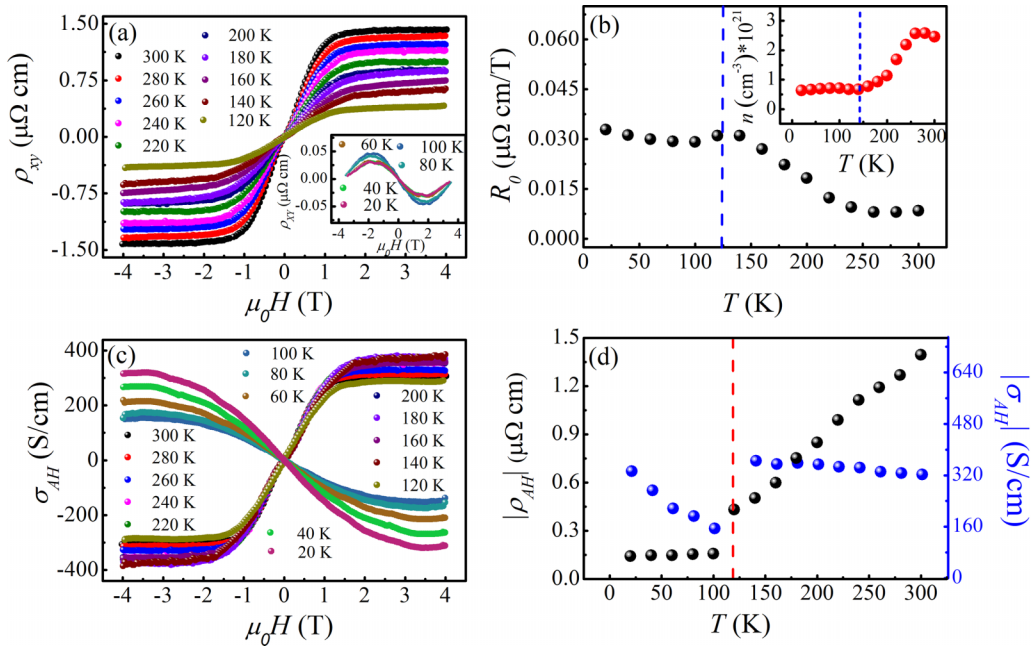

FIG. 3. (a) Hall resistivity curves above SRT. The inset shows the Hall resistivity curves below SRT. (b) Variation of the ordinary Hall coefficient with temperature. The inset shows carrier concentration versus temperature plot. (c) AHC curves at different temperatures. (d) Variation of the AHC and the anomalous Hall resistivity with respect to temperature.

resulting in R_0 also being nearly constant above this temperature. The positive value of R_0 in the whole temperature range (20–300 K) reveals that holes are the dominating charge carriers in transport. The carrier concentration (n) as depicted in the inset of Fig. 3(b), determined by the expression $n = \frac{1}{eR_0}$, was found to be $\sim 0.7\times10^{21}\text{cm}^{-3}$ and $\sim 3\times10^{21}\text{cm}^{-3}$ at 20 K and 300 K, respectively. There is a monotonous change in the value of R_0 and n around T_{SR}, which may be related to the SRT. The AHC has been calculated by using the relation [64,65]

$$\sigma_{\text{AH}} = \frac{\rho_{\text{AH}}}{\rho_{\text{AH}}^2 + \rho_{xx}^2}. \tag{3}$$

The field-dependent ρ_{AH} at different temperatures are calculated by subtracting the ordinary Hall contribution from the field-dependent ρ_{xy}. The calculated field-dependent AHC by using Eq. (3) at different temperatures is shown in Fig. 3(c), which clearly demonstrates the sign change below T_{SR}. The value of AHC at 20 K and 300 K is 322 S/cm and 332 S/cm, respectively. Fig. 3(d) shows that the AHC is nearly independent of the temperature above T_{SR}, whereas below T_{SR}, it shows temperature-dependent behavior as compared to the ρ_{AH}. This observation suggests that above T_{SR}, the intrinsic Berry curvature is primarily attributed to the AHE, whereas the extrinsic skew scattering is the dominating mechanism below T_{SR}.

To quantitatively reveal the contributions of the intrinsic and extrinsic mechanisms to the AHE, the $|\rho_{\text{AH}}|$ versus ρ_{xx} data [black hollow spheres in Fig. 4(a) and inset of Fig. 4(a)] is fitted [red continuous line in Fig. 4(a) and inset of Fig. 4(a)] by using the conventional scaling relation [21,63,66–69]

$$|\rho_{\text{AH}}| = a.\rho_{xx} + b.{\rho_{xx}}^2. \tag{4}$$

where parameters a and b contain information about extrinsic skew scattering and the combined effect of extrinsic side jump and intrinsic contribution, respectively. The fitting by using the preceding scaling relation in a high-temperature region above T_{SR} [see Fig. 4(a)] indicates good fitting, whereas in a low-temperature region below T_{SR} [inset of Fig. 4(a)], the scaling relation shows appreciable deviations from the trend of experimental data, which indicates the breakdown of the conventional scaling relation below T_{SR}. A similar breakdown of the conventional scaling relation in the low-temperature region has been observed in the $Mn_{1.5}Ga$ film, where the ρ_{AH} does not show significant change as a function of the ρ_{xx} [70]. This deviation of the conventional scaling relation from the experimental data has found its root in the negligible temperature-dependent component in the skew scattering mechanism as compared to the impurity component [70].

Tian *et al.* argued that the conventional scaling relation shows significant deviation from the experimental data for those systems, where the temperature-dependent component (phonons) have a negligible effect to the skew scattering mechanism in the AHE compared to the impurity [66]. For such systems, they have derived a new scaling relation ($|\rho_{\text{AH}}| = a'.\rho_{xx0} + b.\rho_{xx}^2$) from the conventional scaling relation, after considering the phonon and impurity as an independent source of the skew scattering mechanism ($a.\rho_{xx} = a'.\rho_{xx0} + a''.\rho_{xxT}$, where ρ_{xx0} and ρ_{xxT} are the residual resistivity and phonon-induced resistivity, respectively) and taking the coefficient $a'' \approx 0$ for the negligible phonon contribution in the skew scattering [71]. This new scaling relation is widely termed as the *TYJ scaling relation* [66,72–74].

Therefore, we have used the TYJ scaling relation in the low-temperature region of the MnSb compound, where ρ_{AH} does not exhibit significant variation with the ρ_{xx}. Remarkably, we found a good fit [blue continuous line in Fig. 4(b)],

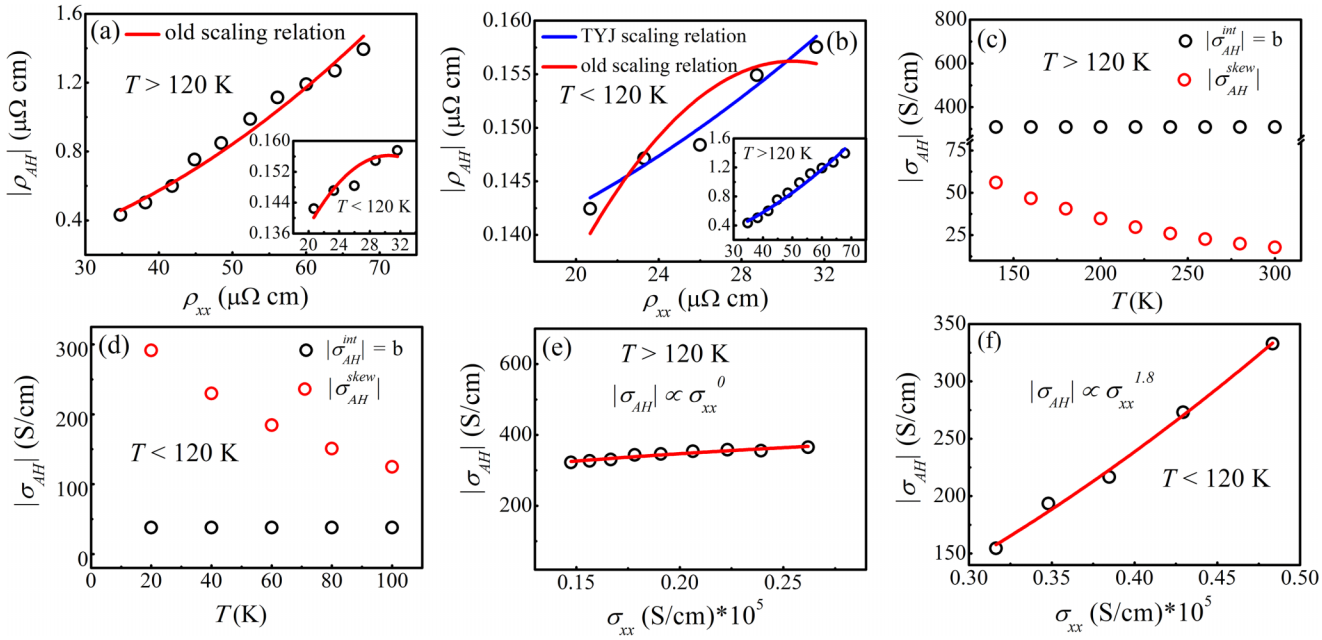

FIG. 4. (a) Fitting of anomalous Hall resistivity ($|\rho_{AH}|$) vs longitudinal resistivity (ρ_{xx}) data above the SRT temperature (T_{SR}) using the conventional scaling relation. The inset shows the same fitting below T_{SR}. The black hollow spheres and the red continuous line represent the experimental data and the fitted curve obtained by the conventional scaling, respectively. (b) Comparison between the fitting of $|\rho_{AH}|$ vs ρ_{xx} data below T_{SR} using conventional scaling and TYJ scaling relations. The inset shows the fitting of $|\rho_{AH}|$ vs ρ_{xx} data above T_{SR} using the conventional scaling relation. The black hollow spheres and the red and blue continuous lines represent the experimental data and the fitted curves obtained by conventional scaling and TYJ scaling, respectively. (c), (d) Different contributions in AHC (σ_{AH}) above and below T_{SR}, respectively. (e), (f) Variation of σ_{AH} with longitudinal conductivity (σ_{xx}) above and below T_{SR}, respectively. The black hollow spheres and the red continuous line represent the experimental data and the fitting using the relation $\sigma_{AH} \propto \sigma_{xx}{}^{\alpha}$.

which is clearly reflected by the comparison of the fitted curves obtained by both scaling relations [see Fig. 4(b)]. The TYJ scaling model perfectly follows the experimental data not only below T_{SR} but also above T_{SR}, as shown in the inset of Fig. 4(b). This finding suggests that the extrinsic contribution to skew scattering from the temperature-dependent component is negligible in the case of the MnSb compound and the AHE is originated by impurity-induced skew scattering, and the combined side jump and intrinsic mechanisms. The value of $a'.\rho_{xx0}$ and the coefficient b in the high-temperature region are $\sim 8.86\times10^{-8}$ Ω cm and $\sim$ 310 S/cm, respectively, whereas in the low-temperature region, they are $a'.\rho_{xx0}$ $\sim 1.25\times10^{-7}$ Ω cm and b ~28 S/cm. The value of parameter b contains the contributions in AHC due to both side jump and momentum space Berry curvature. So far, it has been experimentally infeasible to separate the contributions of a side jump and the intrinsic mechanism in AHC. However, the AHC due to the side jump mechanism can be estimated by using an expression $(e^2/(ha)(E_{so}/E_F)$, where E_{so} is the spin-orbit interaction energy and E_F is Fermi energy [68,75,76]. The physical quantities e, h, and a are the electronic charge, Planck's constant, and lattice parameter, respectively. For most of the ferromagnetic metals, E_{so}/E_F is an order of 10^2 [69], and hence a very small contribution of AHC is expected due to a side jump in comparison to the intrinsic part of AHC.

By using the value of $a'\rho_{xx0}$ and coefficient b, we calculated the temperature-dependent magnitude of extrinsic skew scattering AHC ($|\sigma_{AH}^{skew}| = \frac{a'.\rho_{xx0}}{\rho_{xx}^2}$) and the magnitude of intrinsic AHC ($|\sigma_{AH}^{int}| = b$) and plotted it on same scale above and below T_{SR}, as shown in Fig. 4(c) and Fig. 4(d), respectively. We can clearly see that the intrinsic contribution dominates over the skew scattering contribution in the overall AHE in the high-temperature range above T_{SR}. In comparison, the skew scattering contribution is dominating over the intrinsic contribution in a low-temperature region below T_{SR}, which is consistent with the literature [37].

The dominating mechanism in the AHE can be alternatively evaluated by the exponent α using the scaling relation $|\sigma_{AH}| \propto \sigma_{xx}{}^{\alpha}$. In metallic conductors, if $\alpha = 0$, the intrinsic mechanism contributes largely to the AHE [66,75,77,78], and if α is 2, the skew scattering mechanism dominates in AHE [66,67,72,78,79]. The exponent α determined by fitting is ~0.2, close to 0 above T_{SR} [see Fig. 4(e)], whereas below T_{SR}, the α is 1.8, close to 2 [see Fig. 4(f)], which further supports the observation that in a high-temperature region, the AHE is primarily governed by the intrinsic Berry curvature, whereas in the low-temperature region, it mainly originates by an extrinsic skew scattering mechanism. Above T_{SR}, the obtained value of intrinsic AHC along with the sign is about 310 S/cm, whereas below T_{SR}, the value is about–28 S/cm. To explore the possible reason behind the change in sign and magnitude of intrinsic AHC, we performed the first-principles calculations for the different spin configurations expected around T_{SR}.

D. First-principles calculations

The theoretical calculations of the MnSb compound have been carried out by using lattice parameters obtained from the

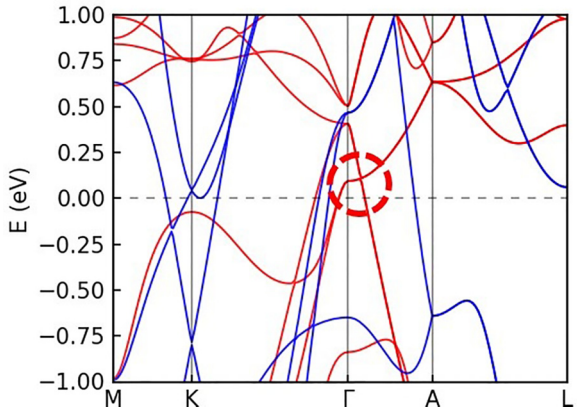

FIG. 5. Spin-polarized electronic band structure of MnSb compound. The red and blue lines represent the majority and minority spin states. The red circles represent the region of our interest around high symmetry point Γ.

Rietveld refinement of XRD data. Our calculated magnetic moment for the stoichiometric MnSb is found to be about 3.43 μ_B/f.u., which is in good agreement with the experimental value. The spin-polarized band structure of the MnSb compound is shown in Fig. 5. The red and blue colors represent the band structure resulting from majority and minority spin states, respectively. An interesting linear touching point between the valence and conduction band is observed along the Γ-A direction from the majority spin states, as shown inside the red circle in Fig. 5. Figs. 6(a) and 6(d) show the crystal structure with the inclusion of magnetic spin of the Mn atom along the *c*-axis and within the *ab*-plane. These structures are built in VESTA software [53]. Since SOC plays an important role in determining the AHC for ferromagnetic materials, we calculated the band structure of MnSb with the SOC and by setting the magnetization along the *c*-axis, as depicted in Fig. 6(b). In the electronic band structure for this magnetic configuration along the *c*-axis, a red circular region highlights band splitting, accompanied by linear band crossings near the Fermi level in proximity to the high symmetry Γ point. This band splitting produces the substantial Berry curvature [see Fig. 6(c)] in the BZ, which may lead to the large intrinsic AHC. To calculate the Berry curvature and intrinsic AHC, the tight binding Hamiltonian is constructed using maximally localized Wannier functions [47,49]. The intrinsic AHC was calculated using the Kubo formula [80]

$$\sigma_{\alpha\beta} = -\frac{e^2}{\hbar}\sum_n \int \frac{d^3k}{(2\pi)^3}\Omega^n_{\alpha\beta} f_n, \tag{5}$$

where Berry curvature Ω can be written as a sum over the eigenstate using the Kubo formula [2]

$$\Omega^n_{\alpha\beta} = i\sum_{n\neq n'} \frac{\langle n|\frac{\partial H}{\partial k^\alpha}|n'\rangle\langle n'|\frac{\partial H}{\partial k^\beta}|n\rangle - (\alpha \leftrightarrow \beta)}{(\epsilon_n - \epsilon'_n)^2}, \tag{6}$$

where $|n\rangle$ and ϵ_n are the energy eigenstate and eigenvalue of Hamiltonian H, respectively. f_n is the Fermi distribution function.

From the integration of the Berry curvature in the BZ, we found the large intrinsic AHC to be about ∼625 S/cm [Fig. 7].

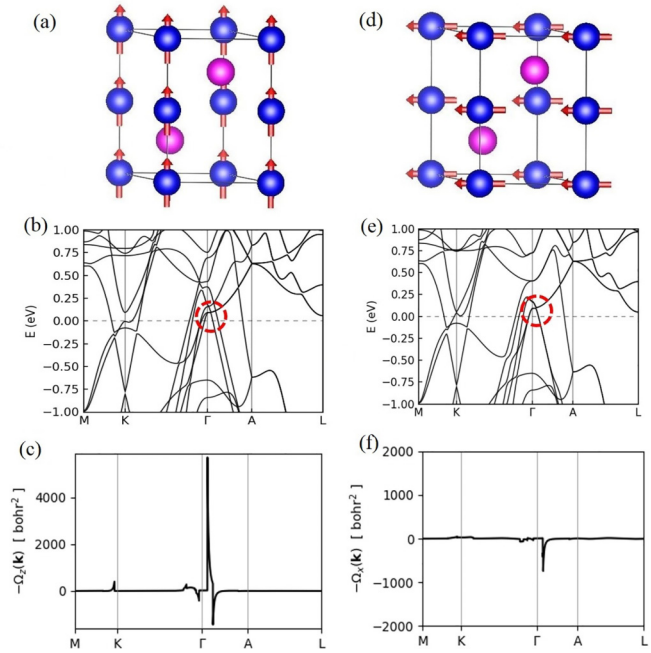

FIG. 6. (a) Crystal structure with the magnetic spins aligned along the *c*-axis. (b) The electronic band structure of MnSb considering the magnetic spin aligned along the *c*-axis. The red circle represents the region of our interest around high symmetry point Γ. (c) Distribution of the Berry curvature along a high symmetry path in the Brillouin zone for the magnetic spin aligned along the *c*-axis. (d) Crystal structure with the magnetic spins within the *ab*-plane. (e) Electronic band structure of MnSb considering the magnetic spin within the *ab*-plane. The red circle represents the region of our interest around high symmetry point Γ. (f) Distribution of the Berry curvature along a high symmetry path in the Brillouin zone for the magnetic spin within the *ab*-plane.

Notably, this value is larger as compared to the other binary compounds [9,22,25]. As this compound undergoes the SRT around 120 K, characterized by the rotation of spins from the *c*-axis to the *ab*-plane [see Fig. 6(d)], we incorporated this phenomenon in the theoretical calculation. We calculated the band structure of MnSb in the presence of SOC by setting the magnetization direction within the *ab*-plane [see Fig. 6(e)]. This differs from the electronic band structure upon considering the magnetization along the *c*-axis. Interestingly, the preexisting band splitting is reduced and the linear touching points near the high symmetry Γ point disappear. The dominated Berry curvature has an opposite sign near the Γ point [see Fig. 6(f)] in contrast to the Berry curvature assuming the magnetic spin in the *c*-direction. Interestingly, we found the intrinsic AHC to be about–162 S/cm [see Fig. 7]. This value is nearly 4 times lower and possesses an opposite sign when compared to the intrinsic AHC calculated considering the magnetic moment in the *c*-direction. The decrease in AHC is attributed to the negligible band splitting as well as the vanishing of linear band crossings, which were present in the band structure when considering the moment in the *c*-direction [see Fig. 6(b)]. The sign reversal of AHC is attributed to the reversal of the sign of Berry curvature, a consequence of the electronic band structure upon rotation of magnetization from

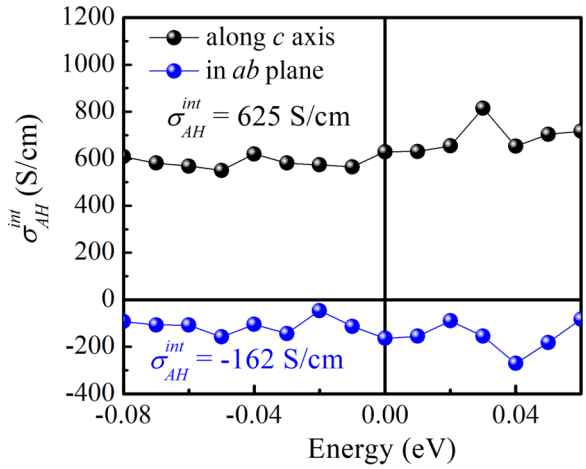

FIG. 7. Variation of intrinsic AHC as a function of energy. The black and blue curves represent the AHC variation with Fermi energy when the magnetization is fixed along the c-direction and *ab*-plane, respectively The Fermi energy is set to 0 eV.

the *c*-axis to the *ab*-plane. The experimentally determined intrinsic AHC values are comparatively smaller than the theoretically calculated ones, although they are of the same order of magnitude.

IV. CONCLUSIONS

We investigated the AHE in the MnSb compound using experimental techniques and theoretical calculations. The detailed scaling analysis of the anomalous Hall data in different temperature regions reflects that an AHE above T_{SR} is mainly governed by the intrinsic Berry curvature and the calculated value of intrinsic AHC ∼310 S/cm. In contrast, below T_{SR}, the AHE mainly originates by skew scattering and the obtained value of intrinsic AHC is about–28 S/cm. The first-principles calculations reveal that sign reversal of AHE is attributed to the Berry curvature modification that emerges from the reconstruction of the electronic band structure when the magnetic moment undergoes rotation from the *c*-axis to the *ab*-plane. Our study yields a compound exhibiting large AHC and offers an insightful comprehension of the anisotropic AHC due to Berry curvature modification, stringently tested through theoretical calculation.

ACKNOWLEDGMENTS

S.S. received financial support from the Science and Engineering Research Board of India through the Core Research Grant (Grant No. CRG/2021/003256) and the UGC DAE CSR project. N.S. and G.K.S. received financial support from the DST INSPIRE scheme.

[1] N. Nagaosa, J. Sinova, S. Onoda, A. H. MacDonald, and N. P. Ong, Anomalous Hall effect, Rev. Mod. Phys. **82**, 1539 (2010).
[2] D. Xiao, M.-C. Chang, and Q. Niu, Berry phase effects on electronic properties, Rev. Mod. Phys. **82**, 1959 (2010).
[3] T. Golod, A. Rydh, P. Svedlindh, and V. M. Krasnov, Anti-ordinary Hall effect near the ferromagnetic quantum phase transition in Ni_xPt_{1-x} thin films, Phys. Rev. B **87**, 104407 (2013).
[4] H. Ohno, D. Chiba, F. Matsukura, T. Omiya, E. Abe, T. Dietl, Y. Ohno, and K. Ohtani, Electric-field control of ferromagnetism, Nature (London) **408**, 944 (2000).
[5] D. Chiba, M. Yamanouchi, F. Matsukura, and H. Ohno, Electrical manipulation of magnetization reversal in a ferromagnetic semiconductor, Science **301**, 943 (2003).
[6] D. Chiba, A. Werpachowska, M. Endo, Y. Nishitani, F. Matsukura, T. Dietl, and H. Ohno, Anomalous Hall effect in field-effect structures of (Ga,Mn)As, Phys. Rev. Lett. **104**, 106601 (2010).
[7] Z. Fang, N. Nagaosa, K. S. Takahashi, A. Asamitsu, R. Mathieu, T. Ogasawara, H. Yamada, M. Kawasaki, Y. Tokura, and K. Terakura, Anomalous Hall effect and magnetic monopoles in momentum space, Science **302**, 92 (2003).
[8] F. D. M. Haldane, Berry curvature on the Fermi surface: Anomalous Hall effect as a topological Fermi-liquid property, Phys. Rev. Lett. **93**, 206602 (2004).
[9] S. Nakatsuji, N. Kiyohara, and T. Higo, Large anomalous Hall effect in a non-collinear antiferromagnet at room temperature, Nature (London) **527**, 212 (2015).
[10] J. Smit and J. Volger, The spontaneous Hall effect in ferromagnetics II, Physica (Amsterdam) **24**, 39 (1958).
[11] L. Berger, Side-jump mechanism for the Hall effect of ferromagnets, Phys. Rev. B **2**, 4559 (1970).
[12] R. Karplus and J. M. Luttinger, Hall effect in ferromagnetics, Phys. Rev. **95**, 1154 (1954).
[13] M. V. Berry, Quantal phase factors accompanying adiabatic changes, Proc. R. Soc. London **392**, 45 (1984).
[14] X. Wang, D. Vanderbilt, J. R. Yates, and I. Souza, Fermi-surface calculation of the anomalous Hall conductivity, Phys. Rev. B **76**, 195109 (2007).
[15] J. M. Luttinger, Theory of the Hall effect in ferromagnetic substances, Phys. Rev. **112**, 739 (1958).
[16] Y. Yao, L. Kleinman, A. H. MacDonald, J. Sinova, and T. Jungwirth, D.-S. Wang, E. Wang, and Q. Niu, First-principles calculation of anomalous Hall conductivity in ferromagnetic bcc Fe, Phys. Rev. Lett. **92**, 037204 (2004).
[17] O. Stejskal, M. Veis, and J. Hamrle, The flow of the Berry curvature vector field, Sci. Rep. **12**, 97 (2022).
[18] N. Lazić, V. Damljanović, and M. Damnjanović, Fully linear band crossings at high symmetry points in layers: Classification and role of spin-orbit coupling and time reversal, J. Phys. A: Math. Theor. **55**, 325202 (2022).
[19] C. Helman, A. Camjayi, E. Islam, M. Akabori, L. Thevenard, C. Gourdon, and M. Tortarolo, Anomalous Hall effect in MnAs: Intrinsic contribution due to Berry curvature, Phys. Rev. B **103**, 134408 (2021).
[20] J. L. Ma, H. L. Wang, X. L. Wang, and J. H. Zhao, Experimental evidence for an anisotropic Berry-phase effect on the anomalous Hall effect in MnAs films, Phys. Rev. B **97**, 064402 (2018).
[21] G. K. Shukla, J. Sau, V. Kumar, M. Kumar, and S. Singh, Band splitting induced Berry flux and intrinsic anomalous Hall

conductivity in the NiCoMnGa quaternary Heusler compound, Phys. Rev. B **106**, 045131 (2022).

[22] A. K. Nayak, J. E. Fischer, Y. Sun, B. Yan, J. Karel, A. C. Komarek, C. Shekhar, N. Kumar, W. Schnelle, J. Kübler, C. Felser, and S. S. P. Parkin, Large anomalous Hall effect driven by a nonvanishing Berry curvature in the noncolinear antiferromagnet Mn_3Ge, Sci. Adv. **2**, e1501870 (2016).

[23] L. Ye, M. Kang, J. Liu, F. von Cube, C. R. Wicker, T. Suzuki, C. Jozwiak, A. Bostwick, E. Rotenberg, D. C. Bell, L. Fu, R. Comin, and J. G. Checkelsky, Massive Dirac fermions in a ferromagnetic kagome metal, Nature (London) **555**, 638 (2018).

[24] J. X. Yin *et al.*, Giant and anisotropic many-body spin–orbit tunability in a strongly correlated kagome magnet, Nature (London) **562**, 91 (2018).

[25] Q. Wang, S. Sun, X. Zhang, F. Pang, and H. Lei, Anomalous Hall effect in a ferromagnetic Fe_3Sn_2 single crystal with a geometrically frustrated Fe bilayer kagome lattice, Phys. Rev. B **94**, 075135 (2016).

[26] T. Kida, L. A. Fenner, A. A. Dee, I. Terasaki, M. Hagiwara, and A. S. Wills, The giant anomalous Hall effect in the ferromagnet Fe_3Sn_2—A frustrated kagome metal, J. Phys.: Condens. Matter **23**, 112205 (2011).

[27] H. Li, B. Zhang, J. Liang, B. Ding, J. Chen, J. Shen, Z. Li, E. Liu, X. Xi, G. Wu, Y. Yao, H. Yang, and W. Wang, Large anomalous Hall effect in a hexagonal ferromagnetic Fe_5Sn_3 single crystal, Phys. Rev. B **101**, 140409(R) (2020).

[28] J. Mukherjee, T. S. Suraj, H. Basumatary, K. Sethupathi, and K. V. Raman, Sign reversal of anomalous Hall conductivity and magnetoresistance in cubic noncollinear antiferromagnet Mn_3Pt thin films, Phys. Rev. Mater. **5**, 014201 (2021).

[29] M. S. Alam, A. Fakhredine, M. Ahmad, P. K. Tanwar, H.-Y. Yang, F. Tafti, G. Cuono, R. Islam, B. Singh, A. Lynnyk, C. Autieri, and M. Matusiak, Sign change of anomalous Hall effect and anomalous Nernst effect in the Weyl semimetal CeAlSi, Phys. Rev. B **107**, 085102 (2023).

[30] R. Ibarra, E. Lesne, B. Sabir, J. Gayles, C. Felser, and A. Markou, Anomalous Hall effect in epitaxial thin films of the hexagonal Heusler MnPtGa noncollinear hard magnet, Adv. Mater. Interfaces **9**, 2201562 (2022).

[31] P. K. Muduli, T. Higo, T. Nishikawa, D. Qu, H. Isshiki, K. Kondou, D. Nishio-Hamane, S. Nakatsuji, and Y.-C. Otani, Evaluation of spin diffusion length and spin Hall angle of the antiferromagnetic Weyl semimetal Mn_3Sn, Phys. Rev. B **99**, 184425 (2019).

[32] D. J. Groenendijk, C. Autieri, T. C. Van Thiel, W. Brzezicki, J. R. Hortensius, D. Afanasiev, N. Gauquelin, P. Barone, K. H. W. Van Den Bos, S. Van Aert, J. Verbeeck, A. Filippetti, S. Picozzi, M. Cuoco, and A. D. Caviglia, Berry phase engineering at oxide interfaces, Phys. Rev. Res. **2**, 023404 (2020).

[33] T. C. van Thiel, W. Brzezicki, C. Autieri, J. R. Hortensius, D. Afanasiev, N. Gauquelin, D. Jannis, N. Janssen, D. J. Groenendijk, J. Fatermans, S. Van Aert, J. Verbeeck, M. Cuoco, and A. D. Caviglia, Coupling charge and topological reconstructions at polar oxide interfaces, Phys. Rev. Lett. **127**, 127202 (2021)

[34] O. Rader, A. Kimura, N. Kamakura, K.-S. An, A. Kakizaki, S. Miyanishi, H. Akinaga, M. Shirai, K. Shimada, and A. Fujimori, Exchange splittings of Mn- and Sb-derived states by spin-resolved valence-band photoemission of MnSb, Phys. Rev. B **57**, R689(R) (1998).

[35] A. Continenza, S. Picozzi, W. T. Geng, and A. J. Freeman, Coordination and chemical effects on the structural, electronic, and magnetic properties in Mn pnictides, Phys. Rev. B **64**, 085204 (2001).

[36] R. Masrour, E. K. Hlil, M. Hamedoun, A. Benyoussef, O. Mounkachi, and H. E. Moussaoui, Electronic and magnetic properties of MnSb compounds, J. Supercond. Nov. Magn. **28**, 1815 (2015).

[37] L. N. Oveshnikov, A. B. Granovsky, A. B. Davydov, A. V. Bogach, A. M. Kharlamova, A. I. Ril, B. A. Aronzon, Magnetic and magnetotransport properties of MnSb polycrystals near equatomic composition, J. Magn. Magn. Mater. **563**, 169873 (2022).

[38] S. F. Marenkin, A. V. Kochura, A. D. Izotov, and M. G. Vasil'ev, Manganese pnictides MnP, MnAs, and MnSb are ferromagnetic semimetals: Preparation, structure, and properties (a survey), Russ. J. Inorg. Chem. **63**, 1753 (2018).

[39] Y. Choi, P. J. Ryan, M. A. McGuire, B. C. Sales, and J.-W. Kim, Giant magnetostriction effect near onset of spin reorientation in MnBi, Appl. Phys. Lett. **112**, 192411 (2018).

[40] A. E. Taylor, T. Berlijn, S. E. Hahn, A. F. May, T. J. Williams, L. Poudel, S. Calder, R. S. Fishman, M. B. Stone, A. A. Aczel, H. B. Cao, M. D. Lumsden, and A. D. Christianson, Influence of interstitial Mn on magnetism in the room-temperature ferromagnet $Mn_{1+\delta}Sb$, Phys. Rev. B **91**, 224418 (2015).

[41] Y. He, J. Gayles, M. Yao, T. Helm, T. Reimann, V. N. Strocov, W. Schnelle, M. Nicklas, Y. Sun, G. H. Fecher, and C. Felser, Large linear non-saturating magnetoresistance and high mobility in ferromagnetic MnBi, Nat. Commun. **12**, 4576 (2021).

[42] S. Singh, B. Dutta, S. W. D'Souza, M. G. Zavareh, P. Devi, A. S. Gibbs, T. Hickel, S. Chadov, C. Felser, and D. Pandey, Robust Bain distortion in the premartensite phase of a platinum-substituted Ni_2MnGa magnetic shape memory alloy, Nat. Commun. **8**, 1006 (2017).

[43] S. Singh, R. Rawat, S. E. Muthu, S. W. D'Souza, E. Suard, A. Senyshyn, S. Banik, P. Rajput, S. Bhardwaj, A. M. Awasthi, R. Ranjan, S. Arumugam, D. L. Schlagel, T. A. Lograsso, A. Chakrabarti, and S. R. Barman, Spin-valve-like magnetoresistance in Mn_2NiGa at room temperature, Phys. Rev. Lett. **109**, 246601 (2012).

[44] P. Giannozzi *et al.* QUANTUM ESPRESSO: A modular and open-source software project for quantum simulations of materials, J. Phys.: Condens. Matter **21**, 395502 (2009).

[45] J. P. Perdew, K. Burke, and M. Ernzerhof, Generalized gradient approximation made simple, Phys. Rev. Lett. **77**, 3865 (1996).

[46] D. R. Hamann, Optimized norm-conserving Vanderbilt pseudopotentials, Phys. Rev. B **88**, 085117 (2013).

[47] N. Marzari and D. Vanderbilt, Maximally localized generalized Wannier functions for composite energy bands, Phys. Rev. B **56**, 12847 (1997).

[48] I. Souza, N. Marzari, and D. Vanderbilt, Maximally localized Wannier functions for entangled energy bands, Phys. Rev. B **65**, 035109 (2001).

[49] G. Pizzi *et al.* Wannier90 as a community code: New features and applications, J. Phys.: Condens. Matter **32**, 165902 (2020).

[50] P. Singh, Structure and growth of MnSb and MnBi thin films, Mater. Lett. **7**, 293 (1988).

[51] P. Radhakrishna and J. W. Cable, Inelastic-neutron-scattering studies of spin-wave excitations in the pnictides MnSb and CrSb, Phys. Rev. B **54**, 11940 (1996).

[52] J. Rodríguez-Carvajal, FullProf, a Rietveld and pattern matching and analysis programs version 2016, Laboratoire Leon Brillouin, CEA-CNRS, France, http://www.ill.eu/sites/fullprof/.

[53] K. Momma and F. Izumi, *VESTA 3* for three-dimensional visualization of crystal, volumetric and morphology data, J. Appl. Crystallogr. **44**, 1272 (2011).

[54] W. Reimers, E. Hellner, W. Treutmann, and G. Heger, Magnetic phase diagram of the system $Mn_{1-x}Cr_xSb$ ($0 \leqslant x \leqslant 1$), J. Phys. C **15**, 3597 (1982).

[55] R. Podloucky, Electronic structure of MnSb, Sol. State Commun. **50**, 763 (1984).

[56] H. Ido, Magnetic properties of mixed crystals with NiAs-type structure, J. Appl. Phys. **57**, 3247 (1985).

[57] X. H. Chen, C. H. Wang, G. Y. Wang, X. G. Luo, J. L. Luo, G. T. Liu, and N. L. Wang, Thermal hysteresis and anisotropy in the magnetoresistance of antiferromagnetic $Nd_{2-x}Ce_xCuO_4$, Phys. Rev. B **72**, 064517 (2005).

[58] P. Sarkar, P. Mandal, K. Mydeen, A. K. Bera, S. M. Yusuf, S. Arumugam, C. Q. Jin, T. Ishida, and S. Noguchi, Role of external and internal perturbations on the ferromagnetic phase transition in $Sm_{0.52}Sr_{0.48}MnO_3$, Phys. Rev. B **79**, 144431 (2009).

[59] J. A. M. Santos, J. F. Collingwood, J. B. Sousa, and S. B. Palmer, Anomalous magnetoresistance near the spin reorientation transition of dilute Gd–Y single crystals, J. Magn. Magn. Mater. **272-276**, E491 (2004).

[60] H. Li, B. Ding, J. Chen, Z. Li, Z. Hou, E. Liu, H. Zhang, X. Xi, G. Wu, and W. Wang, Large topological Hall effect in a geometrically frustrated kagome magnet Fe_3Sn_2, Appl. Phys. Lett. **114**, 192408 (2019).

[61] A. L. Balk, F. Li, I. Gilbert, J. Unguris, N. A. Sinitsyn, and S. A. Crooker, Broadband spectroscopy of thermodynamic magnetization fluctuations through a ferromagnetic spin-reorientation transition, Phys. Rev. X **8**, 031078 (2018).

[62] C. M. Hurd, *The Hall Effect in Metals and Alloys* (Plenum, New York, 1972).

[63] G. K. Shukla, J. Sau, N. Shahi, A. K. Singh, M. Kumar, and S. Singh, Anomalous Hall effect from gapped nodal line in the Co_2FeGe Heusler compound, Phys. Rev. B **104**, 195108 (2021).

[64] K. Manna, L. Muechler, T. H. Kao, R. Stinshoff, Y. Zhang, J. Gooth, N. Kumar, G. Kreiner, K. Koepernik, and R. Car, J. Kübler, G. H. Fecher, C. Shekhar, Y. Sun, and C. Felser, From colossal to zero: Controlling the anomalous Hall effect in magnetic Heusler compounds via Berry curvature design, Phys. Rev. X **8**, 041045 (2018).

[65] B. K. Hazra, M. M. Raja, R. Rawat, A. Lakhani, S. Kaul, and S. Srinath, Effect of disorder on the anomalous Hall conductivity of Co_2FeSi thin films, J. Magn. Magn. Mater. **448**, 371 (2018).

[66] Y. Tian, L. Ye, and X. Jin, Proper scaling of the anomalous Hall effect, Phys. Rev. Lett. **103**, 087206 (2009).

[67] D. Hou, G. Su, Y. Tian, X. Jin, S. A. Yang, and Q. Niu, Multivariable scaling for the anomalous Hall effect, Phys. Rev. Lett. **114**, 217203 (2015).

[68] N. Shahi, A. K. Jena, G. K. Shukla, V. Kumar, S. Rastogi, K. K. Dubey, I. Rajput, S. Baral, A. Lakhani, S.-C. Lee, S. Bhattacharjee, and S. Singh, Antisite disorder and Berry curvature driven anomalous Hall effect in the spin gapless semiconducting Mn_2CoAl Heusler compound, Phys. Rev. B **106**, 245137 (2022).

[69] G. K. Shukla, A. K. Jena, N. Shahi, K. K. Dubey, I. Rajput, S. Baral, K. Yadav, K. Mukherjee, A. Lakhani, K. Carva, S.-C. Lee, S. Bhattacharjee, and S. Singh, Atomic disorder and Berry phase driven anomalous Hall effect in a Co_2FeAl Heusler compound, Phys. Rev. B **105**, 035124 (2022).

[70] L. Zhu, D. Pan, and J. H. Zhao, Anomalous Hall effect in epitaxial $L1_0$-$Mn_{1.5}Ga$ films with variable chemical ordering, Phys. Rev. B **89**, 220406(R) (2014).

[71] A. Crépieux and P. Bruno, Theory of the anomalous Hall effect from the Kubo formula and the Dirac equation, Phys. Rev. B **64**, 014416 (2001).

[72] S.-Y. Yang, Y. Wang, B. R. Ortiz, D. Liu, J. Gayles, E. Derunova, R. Gonzalez-Hernandez, L. Šmejkal, Y. Chen, S. S. P. Parkin, S. D. Wilson, E. S. Toberer, T. McQueen, and M. N. Ali, Giant unconventional anomalous Hall effect in the metallic frustrated magnet candidate, KV_3Sb_5, Sci. Adv. **6**, eabb6003 (2020).

[73] J. Shen, Q. Yao, Q. Zeng, H. Sun, X. Xi, G. Wu, W. Wang, B. Shen, Q. Liu, and E. Liu, Local disorder-induced elevation of intrinsic anomalous Hall conductance in an electron-doped magnetic Weyl semimetal, Phys. Rev. Lett. **125**, 086602 (2020).

[74] J. Shen, S. Zhang, T. Liang, J. Wang, Q. Zeng, Y. Wang, H. Wei, E. Liu, and X. Xu, Intrinsically enhanced anomalous Hall conductivity and Hall angle in Sb-doped magnetic Weyl semimetal $Co_3Sn_2S_2$, APL Mater. **10**, 090705 (2022).

[75] S. Onoda, N. Sugimoto, and N. Nagaosa, Intrinsic versus extrinsic anomalous Hall effect in ferromagnets, Phys. Rev. Lett. **97**, 126602 (2006).

[76] P. Nozieres and C. Lewiner, A simple theory of the anomalous Hall effect in semiconductors, J. Phys. **34**, 901 (1973).

[77] E. Liu *et al.* Giant anomalous Hall effect in a ferromagnetic kagome-lattice semimetal, Nat. Phys. **14**, 1125 (2018).

[78] H. Siddiquee, C. Broyles, E. Kotta, S. Liu, S. Peng, T. Kong, B. Kang, Q. Zhu, Y. Lee, L. Ke, H. Weng, J. D. Denlinger, L. A. Wray, and S. Ran, Breakdown of the scaling relation of anomalous Hall effect in Kondo lattice ferromagnet USbTe, Nat. Commun. **14**, 527 (2023).

[79] F. H. Yu, T. Wu, Z. Y. Wang, B. Lei, W. Z. Zhuo, J. J. Ying, and X. H. Chen, Concurrence of anomalous Hall effect and charge density wave in a superconducting topological kagome metal, Phys. Rev. B **104**, L041103 (2021).

[80] M. Gradhand, D. V. Fedorov, F. Pientka, P. Zahn, I. Mertig, and B. L. Györffy, First-principle calculations of the Berry curvature of Bloch states for charge and spin transport of electrons, J. Phys.: Condens. Matter **24**, 213202 (2012).